Differential multipole method for microstructured optical fibers

S. Campbell, R. C. McPhedran, and C. Martijn de Sterke

School of Physics, Centre of Excellence for Ultrahigh-bandwidth Devices for Optical Systems, University of Sydney, Sydney, New South Wales 2006, Australia

L. C. Botten

School of Mathematical Sciences, Centre of Excellence for Ultrahigh-bandwidth Devices for Optical Systems, University of Technology, Sydney, New South Wales 2007, Australia

Received March 29, 2004; accepted June 28, 2004

We describe the differential multipole method, an extended multipole method used to calculate the modes of microstructured optical fibers with noncircular inclusions. We use a multipole expansion centered on each inclusion and a differential method to calculate the scattering properties of the individual inclusions. Representative results for a fiber with one ring of elliptical inclusions are presented, and a direct comparison is made with an existing method. The new method is also applied to a microstructured optical fiber with seven rings of elliptical inclusions, which is found, in effect, to support a single polarization of the fundamental mode.

OCIS codes: 060.2280, 060.2400, 060.4510.

1. INTRODUCTION

Microstructured optical fibers, or MOFs, come in a wide range of geometries with a number of different guiding mechanisms. The majority of existing MOFs consist of an array of low-index inclusions arranged around a high-index core, where light is guided through a similar mechanism to the total internal reflection in conventional fibers. Other MOF geometries include periodic arrangements of high- or low-index inclusions around a low index or air core, where confinement is due to coherent Bragg scattering.

Modeling these fibers presents a number of challenges: They generally lack rotational symmetry, have large refractive-index contrasts, and require full vector models when high accuracy or vector properties, such as birefringence, are required. Predicting the confinement loss in MOFs has also presented significant challenges. The most widely used technique, the plane-wave method, defines the MOF in a supercell and imposes periodic boundary conditions. Because of this, confinement loss cannot be calculated because the finite geometry has been replaced with an infinite one.

Several methods that are capable of calculating both the propagation constants and the confinement losses have been reported in the literature. With beam propagation methods,[1–3] the scalar or vector wave equation is used to propagate an input pulse along a fiber, from which the guided modes' propagation constants can be determined. Although beam propagation methods are applicable to a wide class of geometries and can calculate loss, the method requires significant computational resources to achieve modest accuracy in loss calculations.

With the adjustable boundary condition (ABC) method[4] a finite-difference discretization is used in the radial direction and a Fourier decomposition is used in the azimuthal direction. The method correctly determines the radiating fields outside the boundary, so it can calculate the loss of the modes for arbitrary fiber geometries. High accuracy can be achieved with this method.

In the multipole method[5,6] each dielectric boundary in the system is treated as a source of radiating fields. In current implementations for circular inclusions, the method achieves high accuracy and rapid convergence, with modest computational resources. Systems with large numbers of inclusions can be modeled, and for structures with discrete rotational symmetries the computational overhead is further reduced by exploitation of the symmetry properties of the modes. The method is limited to nonintersecting circular inclusions, and convergence problems arise as the spacing between the inclusions decreases.

In this paper we extend the multipole method to MOFs with noncircular inclusions through use of a fast Fourier factorization (FFF) method[7,8] to calculate the scattering properties of the individual inclusions. Some accuracy and speed are sacrificed in pursuit of generality; however, it is still well suited to a desktop environment. The multipole method requires minimal reformulation for noncircular inclusions, and existing implementations of the method require the replacement of only a single routine. The new method is suitable for most needs, retaining the strengths of the multipole method with increased generality.

In this paper we combine two existing techniques, so only the details sufficient to outline the differential multipole method (DMM) formulation are presented. Further details can be found in the original publications.[5–8]

After the formulation is introduced, the convergence of the method is discussed, and a direct comparison is made with the ABC method for a fiber with six elliptical inclusions. The method is then applied to a MOF with seven rings of elliptical inclusions, which is seen to support, effectively, a single polarization of the fundamental mode. This fiber has similar dimensions to a recently fabricated fiber, as reported by Issa *et al.*,[9] and so represents a realistic design.

0740-3224/2004/111919-10$15.00

2. FORMULATION

Here the formulation of the DMM is presented. First the multipole method for MOFs is introduced to establish the context for the required extensions to noncircular inclusions. Because of the decoupling between the inclusions' position and shape in the multipole method, no assumptions are necessary in the formulation as to the inclusions cross-sectional geometry, which enters through the reflection matrix **R**. The reflection matrix relates the incident and scattered fields for an inclusion. For circular inclusions this matrix is diagonal and known analytically; for noncircular inclusions, calculating the reflection matrix requires a numerical integration. The structure and qualitative calculation of the reflection matrix is described in Subsection 2.B, and the formulation of the numerical integration is described in Subsection 2.C. Unless defined otherwise, in this paper lower-case letters in bold represent vectors and capital letters in bold represent matrices.

A. Multipole Formulation

The geometry consists of a finite number N_c of inclusions of refractive index n_l, where l refers to the lth inclusion, and all inclusions are oriented parallel to the z axis and embedded in a background material of refractive index n_e. The inclusions are sufficiently separated so that an escribed circle that completely encloses each inclusion without intersecting any other escribed circle can be drawn, as shown in Fig. 1. For circular inclusions this reduces to the requirement for nonintersecting inclusions in the original formulation. Outside the microstructured interior of the fiber the MOF is enclosed by a jacket material of possibly complex refractive index. Here the jacket is not included explicitly; however, we indicate where it enters the formulation.

All field components are taken to have an $\exp i(\beta z - \omega t)$ dependence. Here β is the propagation constant of the mode and ω is the angular frequency of the mode, which is related to the free-space wave number by $\omega = ck_0$. The effective index of a mode is defined as $n_{\mathrm{eff}} = \beta/k_0$. The imaginary part of the effective index is related to the confinement loss in decibels per kilometer by

$$\mathrm{loss(dB/km)} = \frac{20}{\ln(10)}\frac{2\pi}{\lambda} n_{\mathrm{eff}}^{i} \times 10^{9}, \qquad (1)$$

where λ is in micrometers. Specifying the E_z and H_z field components is sufficient to specify the fields in the structure, with the other field components following from Maxwell's equations.[10] In the background the refractive index n_e is constant, so the longitudinal field components E_z and H_z satisfy a radial Helmholtz equation $(\nabla_r^2 + \kappa^2)\psi = 0$ with $\kappa = k_\perp^e = (k_0^2 n_e^2 - \beta^2)^{1/2}$ in the background.

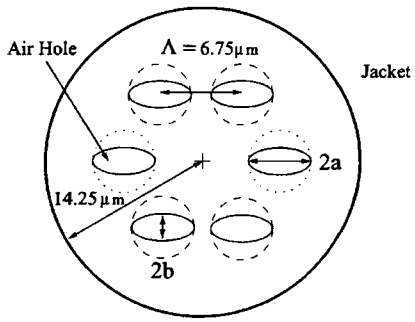

Fig. 1. Schematic of the MOF considered. Λ is the center-to-center separation, a is the semimajor inclusion axis, and b is the semiminor inclusion axis, where $b = \eta a$. The case of $\eta = 1$ is denoted by the dashed and dotted circles and defines the escribed circle for each inclusion. The difference between the dashed and dotted circles is discussed in Section 3.

Inside each inclusion the fields satisfy the same equation, with $\kappa = k_\perp^l = (k_0^2 n_l^2 - \beta^2)^{1/2}$. Local field expansions for E_z and H_z are made about the lth inclusion in the coordinate system $\mathbf{r}_l = (r_l, \theta_l)$ in cylindrical harmonic functions, valid in an annulus extending from the escribed circle of the inclusion to the escribed circle of the nearest inclusion:

$$E_z^{\,l} = \sum_{m=-M}^{M} [a_m^{E,l} J_m(k_\perp^e r_l) + b_m^{E,l} H_m^{(1)}(k_\perp^e r_l)] \exp(im\theta_l), \qquad (2)$$

where $J_m(z)$ is the Bessel function of order m, $H_m^{(1)}(z)$ is the Hankel function of the first kind of order m, and a similar expression applies for the magnetic field. The expansions are truncated from $-M$ to M. The J_m terms represent the regular incident part of the E_z field for inclusion l, and the $H_m^{(1)}$ terms represent the outgoing wave part of the field. At each inclusion, the reflection matrix connects the outgoing waves and the standing waves: $\mathbf{b}^l = \mathbf{R}^l \mathbf{a}^l$, where $\mathbf{a}^l$ denotes the regular part of the field in the partitioned vector notation $\mathbf{a}^l = [\mathbf{a}^{E,l^T} \mathbf{a}^{H,l^T}]^T$, T denotes transposition, and $\mathbf{b}^l$ denotes the outgoing part of the field.

A global description of the fields was introduced by Wijngaard,[11–13] who reasoned that the regular part of the field $\mathbf{a}^l$, in the annulus surrounding the lth inclusion, is due to the outgoing contributions from all other inclusions $\{\mathbf{b}^j\}_{j\neq l}$ and a standing wave from the jacket, if present (but which is omitted here),

$$E_z = \sum_{j\neq l}^{N_c} \sum_{m=-M}^{M} b_m^{E,j} H_m^{(1)}(k_\perp^e r_l) \exp(im\theta_l), \qquad (3)$$

and similarly for the magnetic field.

A mode exists when the outgoing waves $\mathbf{b} = [\mathbf{b}^{1,T} \ldots \mathbf{b}^{N_c,T}]^T$ and standing waves $\mathbf{a} = [\mathbf{a}^{1,T} \ldots \mathbf{a}^{N_c,T}]^T$, in partitioned vector notation, for all

inclusions are self-consistent, that is, when the local expansion of Eq. (2) and the global expansion of Eq. (3) are equivalent. To relate the different terms with different origins in these expansions, we use Graf's addition theorem,[14] which introduces change of basis matrices. This consistency condition is stated mathematically as the field identity:

$$[\mathbf{I} - \mathbf{R}(\mathbf{H} + \mathbf{S})]\mathbf{b} = \mathbf{0}, \tag{4}$$

where $\mathbf{R} = \mathrm{diag}(\mathbf{R}^l)$, $\mathbf{H}$ is a change of a basis matrix, and the $\mathbf{S}$ matrix represents the interactions between the inclusions, and with the jacket if present. Modes correspond to the values of n_{eff} where the determinant of the matrix $[\mathbf{I} - \mathbf{R}(\mathbf{H} + \mathbf{S})]$ vanishes, with the corresponding null-space vector $\mathbf{b}$ characterizing the modal fields. The numerical procedure to find the modes is described by White *et al.*[5] and Kuhlmey *et al.*[6]

B. Determination of $\mathbf{R}^l$

Calculating the reflection matrices, which relate the incident field to the scattered field, requires that we match the field expansions valid inside and outside the inclusion. For circular inclusions this amounts to application of the electromagnetic boundary conditions—the continuity of the tangential components of the electric and magnetic fields. Consider Figs. 2(a) and 2(b), which show a circular and noncircular inclusion with refractive index n_l in cross section, respectively, where the solid curves denote the dielectric interfaces. Two circles, C_1 the inscribed circle and C_2 the escribed circle, were drawn such that they touch the inside and outside surface of each inclusion, respectively. For the circular inclusion the inscribed and escribed circles are depicted separately; however, in reality they are coincident.

The field expansions valid on the annulus surrounding the inclusion that includes the escribed circle was given in Eq. (2). The inscribed circle is in a uniform medium and does not contain any sources, so the field expansion has the form

$$E_z^l = \sum_{m=-M}^{M} c_m^{E,l} J_m(k_\perp^l r_l)\exp(im\theta_l). \tag{5}$$

At this point we also introduce a Fourier series expansion for each component of the electric and magnetic fields around the lth inclusion, e.g.,

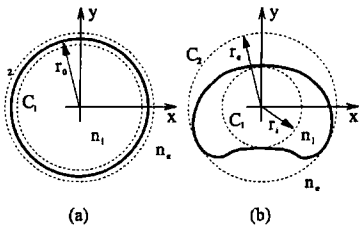

Fig. 2. Comparison between a circular and a noncircular inclusion. The circles C_1 and C_2 touch the inside and outside of each inclusion, respectively, and have radii r_i and r_e for the noncircular inclusion and radius r_0 for the circular inclusion. The lth inclusion has refractive index n_l and the background n_e.

$$E_z^l = \sum_{m=-M}^{M} e_{z,m}(r)\exp(im\theta_l), \tag{6}$$

where $e_{z,m}(r)$ is the mth Fourier coefficient of the z component of the electric field, with similar expansions and expansion coefficients for the other field components. We also introduce vectors of the form $\mathbf{e}_z$ of length $2M + 1$, whose ith element is $e_{z,i}(r)$.

For the circular inclusion the escribed and inscribed circles are coincident, and matching the field expansions requires that we impose continuity conditions on the tangential field components on the dielectric boundary. We do this by equating the Fourier coefficients of the z and θ field components, where θ is the azimuthal angle. The E_θ and H_θ field expansions are calculated with Maxwell's equations[10] from the z field components. Introducing the partitioned vector of Fourier coefficients $\mathbf{v}^l(r) = [\mathbf{e}_z^{l,T}\ \mathbf{h}_z^{l,T}\ \mathbf{e}_\theta^{l,T}\ \mathbf{h}_\theta^{l,T}]^T$, where T denotes transposition, and the matrices $\mathbf{P}_e^l$ and $\mathbf{P}_i^l$ that relate the Fourier series on the escribed and inscribed circles, respectively, for the lth inclusion

$$\mathbf{v}^l(r_e) = \mathbf{P}_e^l\begin{bmatrix}\mathbf{a}^l\\ \mathbf{b}^l\end{bmatrix}, \tag{7}$$

$$\mathbf{v}^l(r_i) = \mathbf{P}_i^l\mathbf{c}^l, \tag{8}$$

the matching conditions become

$$\mathbf{v}^l(r_e) = \mathbf{v}^l(r_i), \tag{9}$$

$$\mathbf{P}_e^l\begin{bmatrix}\mathbf{a}^l\\ \mathbf{b}^l\end{bmatrix} = \mathbf{P}_i^l\mathbf{c}^l. \tag{10}$$

The matrices $\mathbf{P}_i^l$ and $\mathbf{P}_e^l$ are given in Appendix A.

For noncircular inclusions the inscribed and escribed circles are not coincident; and to relate the multipole amplitudes on the inscribed and escribed circles, a numerical integration is required. An ordinary differential equation (ODE) in the Fourier coefficients of the z and θ components of the fields is formed from Maxwell's equations, where $\mathbf{O}$ is a linear operator defined in Appendix B:

$$\frac{\mathrm{d}}{\mathrm{d}r}\mathbf{v}^l(r) = \mathbf{O}\mathbf{v}^l(r). \tag{11}$$

Because the problem is linear, integration of this ODE from the inscribed to the escribed circle yields a matrix $\mathbf{N}^l$ that represents the propagation of the fields from the inscribed circle to the escribed circle:

$$\mathbf{v}^l(r_e) = \mathbf{N}^l\mathbf{v}^l(r_i). \tag{12}$$

We can now equate the analytic [Eq. (7)] and numerical [Eq. (12)] expressions for the fields on the escribed circle:

$$\mathbf{v}^l(r_e) = \mathbf{P}_e^l\begin{bmatrix}\mathbf{a}^l\\ \mathbf{b}^l\end{bmatrix} = \mathbf{N}^l\mathbf{v}^l(r_i) = \mathbf{N}^l\mathbf{P}_i^l\mathbf{c}^l, \tag{13}$$

from which the reflection matrix follows when we multiply through by $\mathbf{P}_e^{l,-1}$ and introduce two 2×2 block matrices $\mathbf{Q}_1^l$ and $\mathbf{Q}_2^l$ that are the upper and lower partitions of the matrix $\mathbf{P}_e^{l,-1}\mathbf{N}^l\mathbf{P}_i^l$. Equation (13) becomes

$$\begin{bmatrix}\mathbf{a}^l\\ \mathbf{b}^l\end{bmatrix} = \mathbf{P}_e^{l,-1}\mathbf{N}^l\mathbf{P}_i^l(\mathbf{c}^l), \tag{14}$$

$$= \begin{bmatrix}\mathbf{Q}_1^l\\ \mathbf{Q}_2^l\end{bmatrix}(\mathbf{c}^l). \tag{15}$$

Eliminating the interior $\mathbf{c}_l$ coefficients yields the reflection matrix

$$\mathbf{b}^l = \mathbf{Q}_2^l\mathbf{Q}_1^{l,-1} = \mathbf{R}^l\mathbf{a}^l. \tag{16}$$

C. Numerical Solution of the Scattering Problem

Here we detail the construction and solution of ODE [Eq. (11)] using a FFF method,[7,8] a differential equation method originally developed for the modeling of diffraction gratings but which is applicable to any periodic boundary-value problem. Differential equation methods project Maxwell's equations onto a complex Fourier series, such that the propagation equations reduce to a set of coupled linear ordinary differential equations in the unknown expansion coefficients of the fields. Compared with conventional differential equation methods, the FFF method achieves much faster convergence of the Fourier series for the fields. This is done through use of the factorization rules presented by Li,[15] which address the problem of convergence of the Fourier series for three cases of products of two periodic discontinuous functions. This problem arises in dielectrics when the product between the electric field and the refractive index squared must be expanded. For example, although both E_{normal} and n^2, where n is the refractive index, are discontinuous functions at a dielectric interface, their product is continuous. For discontinuous periodic functions without concurrent jump discontinuities, Laurent's rule[15] yields Fourier series with the best possible convergence. For complementary jump discontinuities, where each function is individually discontinuous but that together have a continuous product, the inverse rule[15] is used.

1. *Factorization Rules*

Laurent's rule is the standard technique used to expand the product of two arbitrary functions in Fourier series. For two functions f and g, the nth Fourier coefficient of their product fg is given by

$$(fg)_n = \sum_{m=-\infty}^{\infty} f_{n-m}g_m = \sum_{m=-\infty}^{\infty} g_{n-m}f_m, \tag{17}$$

where f_n and g_n are the nth Fourier coefficients of the functions f and g. For an infinite number of Fourier coefficients, Eq. (17) is exact; however, its validity is not obvious when the Fourier series are truncated. For functions without concurrent jump discontinuities, rigorous mathematical arguments[7] show that Laurent's rule is the best way to factor the function product when the series are truncated. Designating $[g]$ to be the vector $[g]_n = g_n$ and $[[f]]$ to be the Toeplitz matrix whose (n, m) entry is f_{n-m}, where $n, m \in (-M, M)$, Eq. (17) becomes

$$[fg] = [[f]][g]. \tag{18}$$

When f and g are individually discontinuous but have a continuous product, the inverse rule[15] is used:

$$[fg] = [[1/f]]^{-1}[g], \tag{19}$$

which is obtained when we apply Laurent's rule to $(1/f) \times (fg) = g$ and invert $[[1/f]]$. Laurent's rule can be applied because (fg) is a continuous function at the discontinuities in f and g by definition, and so the product $(1/f)(fg)$ is without concurrent jump discontinuities.

We want to work with vectors of Fourier coefficients of the fields, so in the above examples g is a field component and f is associated with a material property.

2. *Ordinary Differential Equation Construction with the Fast Fourier Factorization Method*

The formulation of ODE [Eq. (11)] with the FFF method for the particular problem of scattering of light from a dielectric inclusion of arbitrary cross section is given in full by Nevière and Popov.[8] The electric and magnetic field vectors are denoted with superscript vectors, and any symbol in bold follows the conventions of the previous sections, with bold lower-case letters representing vectors and bold capitals representing matrices. The derivation begins with the two steady-state Maxwell curl equations in a dielectric:

$$\nabla \times \vec{E} = ik_0\vec{K}, \tag{20}$$

$$\nabla \times \vec{K} = -ik_0(n^2\vec{E}), \tag{21}$$

where $\vec{K} = Z_0\vec{H} = (\mu_0/\epsilon_0)^{1/2}\vec{H}$ is a scaled magnetic field. Note the product of the refractive index squared and the electric field in Eq. (21). In component form we have six equations in the six field components, and expanding the fields and refractive index in a complex Fourier series at r in an $\exp(im\theta)$ basis we obtain a set of $6 \times (2M + 1)$ equations if the Fourier series of the fields from $-M$ to M are included. In Eq. (21), the function products $[n^2E_r]$, $[n^2E_\theta]$, and $[n^2E_z]$ must be factorized to be expressed as functions of $[E_r]$, $[E_\theta]$, and $[E_z]$. This is done with the FFF method.

In view of factorizing the tangential and normal components of the electric field, we introduce the unit normal $\vec{N}$ to a closed curve that can be described by the function $f(r, \theta) = r - g(\theta) = 0$, where g is a single-valued function:

$$\vec{N} = (\vec{\nabla}f)/|\vec{\nabla}f|. \tag{22}$$

Defining $\vec{E}_N = \vec{N}(\vec{N} \cdot \vec{E})$, the normal component of the electric field, and $\vec{E}_T = \vec{E} - \vec{E}_N$, the tangential component of the electric field, we can express $[n^2\vec{E}]$ as

$$[n^2\vec{E}] = [n^2\vec{E}_T + n^2\vec{E}_N]. \tag{23}$$

The product $n^2\vec{E}_T$ is between a discontinuous and continuous function, so we apply the first factorization rule, Laurent's rule. The product $n^2\vec{E}_N$ is between two discontinuous functions that have a continuous product, so we apply the inverse rule. Equation (23) becomes

$$[n^2\vec{E}] = [[n^2]][\vec{E}_T] + \left[\left[\frac{1}{n^2}\right]\right]^{-1}[\vec{E}_N]. \tag{24}$$

Substituting for the tangential and normal components of the fields and introducing a matrix $\mathbf{Q}_{n^2}$, whose elements are given in Appendix B, we obtain

$$[n^2\vec{E}] = \mathbf{Q}_{n^2}[\vec{E}] = \begin{bmatrix} \mathbf{Q}_{n^2,rr} & \mathbf{Q}_{n^2,r\theta} & 0 \\ \mathbf{Q}_{n^2,\theta r} & \mathbf{Q}_{n^2,\theta\theta} & 0 \\ 0 & 0 & \mathbf{Q}_{n^2,zz} \end{bmatrix} [\vec{E}]. \tag{25}$$

We can now obtain expressions for $[E_r]$, $[E_\theta]$, and $[E_z]$, although here we show only the result for $[E_r]$. From Eq. (25) we can see that

$$[n^2E_r] = \mathbf{Q}_{n^2,rr}[E_r] + \mathbf{Q}_{n^2,r\theta}[E_\theta], \tag{26}$$

and so using

$$i\alpha_\theta\frac{[K_z]}{r} - i\beta[K_\theta] = -ik_0[n^2E_r] \tag{27}$$

from the second Maxwell curl equation, we obtain

$$[E_r] = \mathbf{Q}_{n^2,rr}^{-1}\{[n^2E_r] - \mathbf{Q}_{n^2,r\theta}[E_\theta]\}, \tag{28}$$

$$= \mathbf{Q}_{n^2,rr}^{-1}\left\{\frac{\beta[K_\theta] - \frac{1}{r}\mathbf{M}\alpha_\theta[K_z]}{k_0} - \mathbf{Q}_{n^2,r\theta}[E_\theta]\right\}. \tag{29}$$

We can similarly obtain expressions for $[E_\theta]$ and $[E_z]$. Having done so we obtain six expressions in $[E_r]$, $[E_\theta]$, $[E_z]$, $[K_r]$, $[K_\theta]$, and $[K_z]$. After eliminating $[E_r]$ and $[K_r]$, we are left with four expressions in $[E_\theta]$, $[E_z]$, $[K_\theta]$, and $[K_z]$ that involve only derivatives with respect to r:

$$\frac{\mathrm{d}}{\mathrm{d}r}\begin{bmatrix}[E_z]\\[K_z]\\[E_\theta]\\[K_\theta]\end{bmatrix} = \mathbf{O}\begin{bmatrix}[E_z]\\[K_z]\\[E_\theta]\\[K_\theta]\end{bmatrix}, \tag{30}$$

or in the notation of Subsection 2.B,

$$\frac{\mathrm{d}}{\mathrm{d}r}\mathbf{v}^l(r) = \mathbf{O}\mathbf{v}^l(r),$$

where the coefficient matrix $\mathbf{O}$ is given in Appendix B.

Integrating this ODE with $\mathbf{v}^l(r) = \mathbf{e}^i$, where $(\mathbf{e}^i)_j = 1$ if $j = i$ and zero otherwise, yields the ith column of the matrix $\mathbf{N}^l$ introduced in Eq. (12). Once $\mathbf{N}^l$ has been calculated, the reflection matrix $\mathbf{R}^l$ in Eq. (16) can be calculated when we apply the matching conditions in Eq. (13).

If Li's factorization rules had not been applied, the matrix $\mathbf{Q}_{n^2}$ would have been a diagonal matrix in the Toeplitz matrix for the refractive index squared $[[n^2]]$, and the system of equations obtained would be much simpler. However, as shown by Nevière and Popov,[8] the convergence is significantly improved when Li's factorization rules are used.

3. NUMERICAL IMPLEMENTATION AND VERIFICATION

A. Numerical Procedure

A FORTRAN code was developed and combined with an existing implementation of the multipole method.[6] When we calculate the reflection matrix for an inclusion, the Toeplitz matrices for the components of the normal $[[N_r^2]]$, $[[N_\theta^2]]$, and $[[N_rN_\theta]]$ are calculated at the beginning of the integration and used throughout. The Toeplitz matrices for the refractive index $[[n^2]]$ and $[[1/n^2]]$ are calculated at each step, and no angular discretization is necessary when the refractive index is piecewise constant. In this case the Toeplitz matrices can be calculated exactly if the refractive-index profile is known analytically. A fourth-order Runge–Kutta algorithm is used to integrate the ODE [Eq. (30)]. Applying the matching conditions yields the reflection matrix for the inclusion. The reflection matrices need to be calculated only for inclusions with a unique geometry, and a simple change of basis operation can be used to find the reflection matrix for an identical inclusion with a different orientation.

B. Convergence

The convergence of the modal effective indices n_{eff} in this implementation depends on the number of multipoles M retained in forming the field identity and the numerical errors introduced into the reflection matrices. As M increases, the agreement between the local expansions and the global expansions improves until the conditioning of the matrices entering the field identity limits the agreement. The numerical differences between the expansions on the inclusions' escribed circles are a strong indication of truncation errors—both the errors introduced when M is too small and the errors due to conditioning when M is large. To characterize the agreement between local and global expansions, Kuhlmey *et al.*[6] introduced

$$W = \frac{\int_{C_2} |E_z^{\mathrm{local}}(\theta_l) - E_z^{\mathrm{Wijngaard}}(\theta_l)|\,\mathrm{d}\theta_l}{\int_{C_2} |E_z^{\mathrm{Wijngaard}}(\theta_l)|\,\mathrm{d}\theta_l}, \tag{31}$$

which is evaluated on the escribed circle of the lth inclusion.

The convergence of the local expansions depends on the number of multipoles. For circular inclusions, the interaction can be represented with relatively few multipoles. For more complex inclusion geometries, the fields scattered by the inclusion have larger angular variations, so more multipoles are required to represent the scattered field. With increasing M, W decreases and the convergence of n_{eff} improves. However, any numerical errors in the reflection matrix cause the effective index to converge to the wrong value, so calculating the reflection matrix accurately is critical. Increasing the spatial resolution in the integration, which is determined only by the number of radial integration steps when the refractive-index profile is known analytically, improves the convergence. The convergence can be further improved when higher-order Fourier coefficients are retained during the reflection matrix calculation, which are discarded when the field identity is formed. This is because in general there is coupling between different orders in the form of convolutions, so performing the numerical integration with extra Fourier coefficients improves the convergence of the lower-order coefficients, and hence the convergence of the modal effective indices.

Table 1. Convergence of n_{eff} with M[a]

$M_{\max}$	$\mathrm{Re}(n_{\mathrm{eff}})$	$\mathrm{Im}(n_{\mathrm{eff}}) \times 10^{-6}$	W_{dot}	W_{dash}
4	1.446419435	2.9437	3.4×10^{-3}	5.5×10^{-3}
5	1.446411348	1.4287	2.0×10^{-3}	4.2×10^{-3}
6	1.446397187	2.1808	2.7×10^{-4}	1.7×10^{-3}
7	1.446396099	2.4601	1.2×10^{-4}	5.4×10^{-4}
8	1.446397463	2.3382	1.1×10^{-4}	3.5×10^{-4}
9	1.446397587	2.3116	4.7×10^{-2}	1.8×10^{-4}

[a] Results are for the polarization of the fundamental mode with the horizontal E_z nodal line, where $\eta = 0.6$. W, from Eq. (31), indicates the agreement between the local and the global expansions and is equal on the dotted and dashed escribed circles in Fig. 1.

In the following, the MOF considered (shown in Fig. 1) has identical inclusions with fixed semimajor axis $a = 2.5\ \mu\mathrm{m}$ and varying semiminor axis $b = \eta a$, with each inclusion separated by a center-to-center distance of $\Lambda = 6.75\ \mu\mathrm{m}$. The ellipticity of the inclusions is defined as the ratio of the minor to the major axis and is given by η. All modes are calculated at the wavelength $\lambda = 1.45\ \mu\mathrm{m}$. The inclusions have refractive index $n_l = 1$, and the background refractive index is $n_e = 1.45$. A jacket with refractive index $n_j = 1.45 + 2.9 \times 10^{-8}$ was included in the calculations; however, the jacket was found to have no effect on the modal effective indices within the precision presented in this subsection. The modes of the equivalent structure with circular inclusions are either singly or doubly degenerate. For $\eta < 1$, all degeneracies are lifted, so here we follow the two perpendicular polarizations of the fundamental modes of the circular structure as η is varied.

Table 1 shows the convergence of the effective index of the E_z polarization with a horizontal nodal line of the fundamental mode as the number of multipoles is varied. The number of multipoles used in the calculation of the reflection matrix is $M = 10$, and η is fixed at 0.6. Included in Table 1 is the W parameter, which indicates the agreement between the local and the global expansions. Because of the modal symmetries, W is equal on the dashed and dotted escribed circles in Fig. 1. The real part of the effective index can be seen to converge to seven significant figures and the imaginary part converges to 2. As the number of multipoles is increased, W decreases; however, at $M = 9$ the agreement between the local and the global expansions begins to deteriorate, because of the conditioning of the matrices that enter the field identity. If the inclusions were circular, the convergence for $M = 9$ is to ten and four significant figures in the real and imaginary parts, respectively, because of the smaller angular variations in the fields scattered by a circular inclusion and the fact that the reflection matrices are known analytically.

A direct comparison was made with the ABC method[4] for the MOF considered here. The effective indices of the two polarizations of the fundamental mode were calculated as a function of η. The effective indices of the different polarizations of the fundamental mode as calculated by the ABC method and the multipole method are presented in Tables 2 and 3. For the DMM, $M = 9$ is used to form the field identity, and $M = 10$ is used to calculate the reflection matrix. Sufficient integration steps were taken such that the convergence was multipole limited. For the ABC model, the radial resolution, which refers to the number of points in the radial direction at which the fields are calculated, was 1000; and the angular resolution, which refers to the truncation of the Fourier series, was 60. Both the ABC results and the DMM results have converged to seven significant figures in the real part of the effective index and converged to two in the imaginary part,[16] which is in agreement with one results.

The methods agree well, with a consistency to six significant figures in $\mathrm{Re}(n_{\mathrm{eff}})$ and one in $\mathrm{Im}(n_{\mathrm{eff}})$, although

Table 2. Comparison between the DMM and the ABC Method for the Polarization of the Fundamental Mode with the Horizontal E_z Nodal Line

η	$\mathrm{Re}(n_{\mathrm{eff}})$	$\mathrm{Im}(n_{\mathrm{eff}})$
1		
DMM	1.445395232	3.1945×10^{-8}
ABC	1.445397228	3.2376×10^{-8}
0.9		
DMM	1.445672782	1.1040×10^{-7}
ABC	1.445672267	1.1191×10^{-7}
0.8		
DMM	1.445929388	3.5723×10^{-7}
ABC	1.445929716	3.7576×10^{-7}
0.7		
DMM	1.446169785	9.8458×10^{-7}
ABC	1.44617215	1.1166×10^{-6}
0.6		
DMM	1.446397587	2.3116×10^{-6}
ABC	1.446404071	2.9339×10^{-6}

Table 3. Comparison between the DMM and the ABC Method for the Polarization of the Fundamental Mode with the Vertical E_z Nodal Line

η	$\mathrm{Re}(n_{\mathrm{eff}})$	$\mathrm{Im}(n_{\mathrm{eff}})$
1		
DMM	1.445395232	3.1945×10^{-8}
ABC	1.445397228	3.2376×10^{-8}
0.9		
DMM	1.445677647	1.3560×10^{-7}
ABC	1.445676964	1.3624×10^{-7}
0.8		
DMM	1.445941057	4.6190×10^{-7}
ABC	1.445941003	4.8042×10^{-7}
0.7		
DMM	1.446189882	1.2755×10^{-6}
ABC	1.4461916	1.4230×10^{-6}
0.6		
DMM	1.446427235	2.9601×10^{-6}
ABC	1.44643281	3.6624×10^{-6}

this is less than the internal convergence of each method. The reason for this is not presently clear and will be the subject of future research. Each individual calculation in Tables 2 and 3 for the DMM required approximately 8 min on an Intel Pentium 4 2.0-GHz computer, with 5 megabytes of memory used. Similar calculations to those above for circular inclusions would take approximately 5 s and use a similar amount of memory. Thus the DMM is an efficient technique to model MOFs in a desktop environment when high accuracy is required. The computational cost of calculating the reflection matrices numerically dominates that of forming and calculating the eigenvalues and eigenvectors of the field identity for small numbers of identical inclusions. However, when the number of inclusions $N_c \approx 25$, the computational cost of calculating the eigenvectors of the field identity begins to become significant; and for larger numbers of inclusions, the main computational overhead is the solution of the field identity for the modal effective indices.

4. MODAL CUTOFFS IN ELLIPTICAL INCLUSION MICROSTRUCTURED OPTICAL FIBERS

For an application of the DMM, we consider a MOF with elliptical inclusions previously studied by Steel and Osgood[17,18] using the plane-wave method. Our motivation for choosing this fiber is to answer an unresolved question regarding the cutoffs of the two polarizations of the fundamental mode. One useful picture of modal cutoffs involves the fundamental space-filling mode (FSM),[19] which in a step-index circular fiber is the radiation mode with the highest effective index. In a MOF geometry the FSM states are the fundamental states of the infinite photonic crystal cladding if the core is absent. In this case a mode is guided in the core of the fiber if the real part β^r of the propagation constant of the mode is greater than the propagation constant of the FSM state and less than the wave number in the core:

$$k_0 n_{\text{core}} > \beta^r > \beta_{\text{FSM}}. \tag{32}$$

The effective index $n_{\text{eff}} = \beta_{\text{FSM}}/k_0$ of the FSM can be thought of as the effective cladding index of the fiber.

In a MOF with elliptical inclusions with the same orientation, the FSM, like the fundamental mode, splits. For certain geometries Steel and Osgood found that the propagation constant of one of the fundamental modes could pass through the FSM with the opposite polarization. They proposed that the mode would become cut off at this point, but were unable to answer this question definitively because of the inability of the plane-wave method to calculate confinement loss. Subsequent modeling by beam propagation was unable to resolve the issue because of the large losses near the modal cutoffs. If the mode did become cut off, the fiber would support only a single polarization of the fundamental mode.

The structure modeled here, inset in Fig. 3, consists of seven rings of elliptical inclusions arranged on a hexagonal lattice. The lattice constant is $\Lambda = 4\ \mu$m, and each inclusion has a major axis of 2.8546 μm and a minor axis of 1.4273 μm, so $b = 0.5a$. The inclusion refractive index is $n_i = 1$, the background refractive index is $n_e = 1.45$, and a jacket with refractive index $n_j = 1.45 + 2.9 \times 10^{-8}$ was included. The jacket was found to have no effect on the modal effective indices. The fabrication of a MOF with elliptical inclusions in which the major hole pitch was 3.82 μm, the inclusions had a major axis of 2.1 μm, and the ratio of major to minor axis was 1.85 was recently reported by Issa *et al.*[9] Thus the fiber modeled here is a realistic design. In the modeling, $M = 9$ multipoles is used in the calculation of the reflection matrices and $M = 7$ is used in the formation of the field identity. In Fig. 3 the real parts of the FSMs and the fundamental modes' effective indices are plotted as a function of the dimensionless frequency $\nu = \omega\Lambda/(2\pi c)$ for consistency with Steel and Osgood.[17,18] The frequency in hertz is given by $f = c\nu/\Lambda$.

At $\nu = 0.7$, the polarization of the fundamental mode with the horizontal E_x nodal line (guided x) passes through the FSM with the vertical E_z nodal line (FSM y). If the mode was to become cut off for lower frequencies, we would expect its confinement loss to increase dramatically for $\nu < 0.7$. Figure 4 is a plot of the imaginary part of the effective index for the two polarizations of the fundamental mode. The confinement loss in decibels per kilometer is given by Eq. (1). We can see that the loss of the guided x mode starts to increase dramatically for $\nu < 0.9$; however, in contrast to the prediction made by Steel and Osgood, the loss curve of the guided x mode is unaffected by the crossing of the FSM y state at $\nu = 0.7$. Furthermore, the loss of the guided x mode is actually smaller than that of the guided y mode. This is because

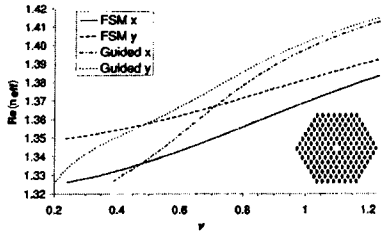

Fig. 3. Real part of the effective index of the fundamental modes and the FSMs of a seven-ring hexagonal MOF (inset) with elliptical inclusions oriented vertically with the major axis.

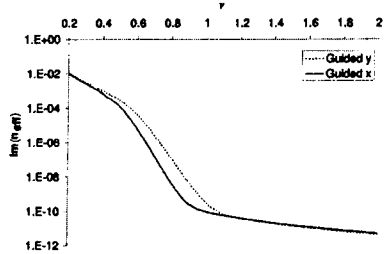

Fig. 4. Imaginary part of the effective index on a log-linear scale of the fundamental modes of a seven-ring hexagonal MOF with elliptical inclusions oriented vertically with the major axis. At $\nu = 0.65$ the ratio of the losses of the guided x mode to the guided y mode is 0.02.

the difference in the effective index of the guided x mode and the FSM x state is larger than the difference between the guided y mode and the FSM y state. In the effective cladding picture the mode with effective index closest to the corresponding effective cladding index would have the higher confinement loss, which is indeed the case here.

More generally, Fig. 4 indicates three different trends in the modal losses. For frequencies $\nu > 1.1$, the confinement loss is small, and both modes have similar propagation constants. In this regime the modes are tightly confined to the core of the fiber. For frequencies $\nu < 0.45$, which from Fig. 3 is the frequency at which each mode crosses its corresponding FSM, the confinement losses are large, and both modes are poorly confined. This agrees well with the effective index model for the modal cutoffs.[20] For frequencies $0.45 < \nu < 1.1$, we can see a transition region where the confinement loss is changing rapidly, and the loss curves for each mode have the same shape. However, because of their relative shift there is a strong polarization-dependent loss. These two asymptotic regions and the transition region closely resemble the predictions of Kuhlmey *et al.*[21] for MOFs with circular inclusions.

At $\nu = 0.83$ the ratio of the confinement losses reaches a maximum of 27, and the confinement losses for the two modes at this frequency are 13.5 and 367 dB/km. This suggests that the fiber would support only a single polarization of the fundamental mode at the wavelength of $\lambda = 4769$ nm. Kubota *et al.*[22] have reported a MOF where the loss ratio between the two polarizations of the fundamental mode is of the order of 8 at a wavelength of $\lambda = 1550$ nm. Measurements indicated that the fiber supported only a single polarization of the fundamental mode. It is likely that a MOF consisting of a hexagonal array of elliptical inclusions could be designed to similar specifications at a wavelength of 1550 nm; however, this question is beyond the scope of this paper.

5. DISCUSSION AND CONCLUSIONS

In this paper we have extended an efficient existing method for modeling MOFs with the multipole method to fiber geometries with noncircular inclusions through use of a FFF method. The DMMs main feature is its use of local expansions about the arbitrary inclusions. The method was shown to be in excellent agreement with an existing method. Applying the method to a fiber with seven rings of elliptical inclusions revealed that the fiber effectively supported a single polarization of the fundamental mode.

One of the features of the FFF method is that it does not lose accuracy with increasing refractive-index contrast. Thus our method will retain its accuracy for chalcogenide and other high-index MOFs under investigation. The refractive indices can also be complex, so material loss can be treated easily.

The formulation here implicitly assumed that the refractive-index profile of the inclusion could be represented by an injective function g, where $r = g(\theta)$. We could overcome this restriction by representing the refractive-index profile as a number of simply connected domains, and inclusions with arbitrary geometry could then be studied.

Finally, more general formulations of the FFF method are applicable to anisotropic media. For example, MOFs with inclusions filled with liquid crystals for tunability could be studied.

APPENDIX A: REFLECTION MATRIX CONSTRUCTION

We consider an arbitrary inclusion as shown in Fig. 2. We use the Fourier series expansions introduced in Eq. (6), with similar expressions for the other field components. To relate the multipole amplitudes to the Fourier coefficients, we must calculate the θ field components using Maxwell's equations[10]:

$$E_\theta(r,\theta) = \frac{i}{k_\perp^2}\left(\frac{\beta}{r}\frac{\partial E_z}{\partial \theta} - k_0\frac{\partial K_z}{\partial r}\right), \tag{A1}$$

$$K_\theta(r,\theta) = \frac{i}{k_\perp^2}\left(\frac{\beta}{r}\frac{\partial K_z}{\partial \theta} + k_0 n^2\frac{\partial E_z}{\partial r}\right), \tag{A2}$$

where n is the appropriate refractive index.

Calculating the E_θ and K_θ field components and equating the Fourier series and multipole expansions on the inscribed circle yields the matrix $\mathbf{P}_i^l$:

$$\begin{bmatrix} \mathbf{e}_z^l(r_i) \\ \mathbf{k}_z^l(r_i) \\ \mathbf{e}_\theta^l(r_i) \\ \mathbf{k}_\theta^l(r_i) \end{bmatrix} = \mathbf{P}_i^l \begin{bmatrix} \mathbf{c}^{E,l} \\ \mathbf{c}^{K,l} \end{bmatrix}, \tag{A3}$$

where

$$\mathbf{P}_i^l = \begin{bmatrix} \mathbf{J}_i & \mathbf{0} \\ \mathbf{0} & \mathbf{J}_i \\ \dfrac{\beta}{k_\perp^{i,2} r_i}\mathbf{M}\mathbf{J}_i & -\dfrac{ik_0}{k_\perp^i}\mathbf{J}_i' \\ \dfrac{ik_0 n_i^2}{k_\perp^i}\mathbf{J}_i' & -\dfrac{\beta}{k_\perp^{i,2} r_i}\mathbf{M}\mathbf{J}_i \end{bmatrix}, \tag{A4}$$

and $\mathbf{M} = \text{diag}(m)$, $\mathbf{J}_i = \text{diag}[J_m(k_\perp^i r_i)]$, and $\mathbf{H}_i = \text{diag}[H_m^{(1)}(k_\perp^i r_i)]$ with similar expressions for $\mathbf{J}_e$ and $\mathbf{H}_e$. The primes denote derivatives with respect to the argument.

Repeating this on the escribed circle yields $\mathbf{P}_e^l$:

$$\begin{bmatrix} \mathbf{e}_z^l(r_i) \\ \mathbf{k}_z^l(r_i) \\ \mathbf{e}_\theta^l(r_i) \\ \mathbf{k}_\theta^l(r_i) \end{bmatrix} = \mathbf{P}_e^l \begin{bmatrix} \mathbf{a}^{E,l} \\ \mathbf{a}^{K,l} \\ \mathbf{b}^{E,l} \\ \mathbf{b}^{K,l} \end{bmatrix}, \tag{A5}$$

where

$$\mathbf{P}_e^l = \begin{bmatrix} \mathbf{J}_e & \mathbf{0} & \mathbf{H}_e & \mathbf{0} \\ \mathbf{0} & \mathbf{J}_e & \mathbf{0} & \mathbf{H}_e \\ \dfrac{\beta}{k_\perp^{e,2} r_e}\mathbf{M}\mathbf{J}_e & \dfrac{ik_0}{k_\perp^e}\mathbf{J}_e{}' & \dfrac{\beta}{k_\perp^{e,2} r_e}\mathbf{M}\mathbf{H}_e & \dfrac{ik_0}{k_\perp^e}\mathbf{H}_e{}' \\ \dfrac{ik_0 n_e^2}{k_\perp^e}\mathbf{J}_e{}' & \dfrac{\beta}{k_\perp^{e,2} r_e}\mathbf{M}\mathbf{J}_e & \dfrac{ik_0 n_e^2}{k_\perp^e}\mathbf{H}_e{}' & \dfrac{\beta}{k_\perp^{e,2} r_e}\mathbf{M}\mathbf{H}_e \end{bmatrix}. \quad \text{(A6)}$$

The last element required is the matrix $\mathbf{N}^l$, which represents the numerical integration from the inscribed to the escribed circles. Equating the analytic and numerical expressions for the fields on the escribed circle, we obtain Eq. (13). Multiplying through by $\mathbf{P}_e^{-1}$ and introducing two 2×2 block matrices $\mathbf{Q}_1$ and $\mathbf{Q}_2$, where

$$\begin{bmatrix} \mathbf{a}^{E,l} \\ \mathbf{a}^{K,l} \\ \mathbf{b}^{E,l} \\ \mathbf{b}^{K,l} \end{bmatrix} = \mathbf{P}_e^{-1}\mathbf{N}^l\mathbf{P}_i \begin{bmatrix} \mathbf{c}^{E,l} \\ \mathbf{c}^{K,l} \end{bmatrix} = \begin{bmatrix} \mathbf{Q}_1 \\ \mathbf{Q}_2 \end{bmatrix} \begin{bmatrix} \mathbf{c}^{E,l} \\ \mathbf{c}^{K,l} \end{bmatrix}, \quad \text{(A7)}$$

allows us to eliminate the interior coefficients $\mathbf{C}^l$ to form the reflection matrix

$$\begin{bmatrix} \mathbf{B}^E \\ \mathbf{B}^K \end{bmatrix} = \mathbf{Q}_2\mathbf{Q}_1^{-1} \begin{bmatrix} \mathbf{A}^E \\ \mathbf{A}^K \end{bmatrix} = \mathbf{R}^l \begin{bmatrix} \mathbf{A}^E \\ \mathbf{A}^K \end{bmatrix}. \quad \text{(A8)}$$

APPENDIX B: ORDINARY DIFFERENTIAL EQUATION CONSTRUCTION AND NUMERICAL INTEGRATION

The matrix $\mathbf{Q}_{n^2}$ follows from Eq. (24), and use of $[[N_\theta^2]] + [[N_r^2]] = \mathbf{I}$, where $\mathbf{I}$ is the identity matrix that follows from the normal being a unit vector. $\mathbf{Q}_{n^2}$ then has the elements

$$\mathbf{Q}_{n^2} = \begin{bmatrix} \mathbf{Q}_{n^2,rr} & \mathbf{Q}_{n^2,r\theta} & \mathbf{0} \\ \mathbf{Q}_{n^2,\theta r} & \mathbf{Q}_{n^2,\theta\theta} & \mathbf{0} \\ \mathbf{0} & \mathbf{0} & \mathbf{Q}_{n^2,zz} \end{bmatrix}, \quad \text{(B1)}$$

where

$$\mathbf{Q}_{n^2,rr} = [[n^2]][[N_\theta^2]] + \left[\left[\frac{1}{n^2}\right]\right]^{-1}[[N_r^2]],$$

$$\mathbf{Q}_{n^2,r\theta} = -\left([[n^2]] - \left[\left[\frac{1}{n^2}\right]\right]^{-1}\right)[[N_r N_\theta]],$$

$$\mathbf{Q}_{n^2,\theta r} = -\left([[n^2]] - \left[\left[\frac{1}{n^2}\right]\right]^{-1}\right)[[N_r N_\theta]],$$

$$\mathbf{Q}_{n^2,\theta\theta} = [[n^2]][[N_r^2]] + \left[\left[\frac{1}{n^2}\right]\right]^{-1}[[N_\theta^2]],$$

$$\mathbf{Q}_{n^2,zz} = [[n^2]].$$

Without Li's factorization rules, $[[1/n^2]]^{-1}$ would be replaced with $[[n^2]]$ and $\mathbf{Q}_{n^2}$ would be a diagonal matrix in $[[n^2]]$.

The coefficient matrix $\mathbf{O}$ from Eq. (30) has the elements

$$\mathbf{O}_{11} = \mathbf{0},$$

$$\mathbf{O}_{12} = -\frac{i\beta}{rk_0}\mathbf{Q}_{n^2,rr}^{-1}\mathbf{M},$$

$$\mathbf{O}_{13} = -i\beta\mathbf{Q}_{n^2,rr}^{-1}\mathbf{Q}_{n^2,r\theta},$$

$$\mathbf{O}_{14} = \frac{i\beta^2}{k_0}\mathbf{Q}_{n^2,rr}^{-1} - ik_0\mathbf{I},$$

$$\mathbf{O}_{21} = \frac{i\beta}{rk_0}\mathbf{M},$$

$$\mathbf{O}_{22} = -\frac{i}{r}\mathbf{Q}_{n^2,\theta r}\mathbf{Q}_{n^2,rr}^{-1}\mathbf{M},$$

$$\mathbf{O}_{23} = -\frac{i\beta^2}{k_0}\mathbf{I} + ik_0(\mathbf{Q}_{n^2,\theta\theta} - \mathbf{Q}_{n^2,\theta r}\mathbf{Q}_{n^2,rr}^{-1}\mathbf{Q}_{n^2,r\theta}),$$

$$\mathbf{O}_{24} = i\beta\mathbf{Q}_{n^2,\theta r}\mathbf{Q}_{n^2,rr}^{-1},$$

$$\mathbf{O}_{31} = \mathbf{0},$$

$$\mathbf{O}_{32} = ik_0\mathbf{I} - \frac{i}{r^2k_0}\mathbf{M}\mathbf{Q}_{n^2,rr}^{-1}\mathbf{M},$$

$$\mathbf{O}_{33} = -\frac{1}{r}\mathbf{I} - \frac{i}{r}\mathbf{M}\mathbf{Q}_{n^2,rr}^{-1}\mathbf{Q}_{n^2,r\theta},$$

$$\mathbf{O}_{34} = \frac{i\beta}{k_0 r}\mathbf{M}\mathbf{Q}_{n^2,rr}^{-1},$$

$$\mathbf{O}_{41} = \frac{i}{r^2k_0}\mathbf{M}^2 - ik_0\mathbf{Q}_{n^2,zz},$$

$$\mathbf{O}_{42} = \mathbf{0},$$

$$\mathbf{O}_{43} = -\frac{i\beta}{rk_0}\mathbf{M},$$

$$\mathbf{O}_{44} = -\frac{1}{r}\mathbf{I}.$$

ACKNOWLEDGMENTS

This research was produced with the assistance of the Australian Research Council (ARC) under the ARC Centres of Excellence program. The Centre for Ultrahigh-bandwidth Devices for Optical Systems is an ARC Centre of Excellence.

The original multipole code was provided by Boris Kuhlmey, who also developed extensions required for non-circular inclusions.

The authors thank Nader Issa for providing the ABC calculations that were used in this paper and Philippe Boyer for providing in-plane scattering results that were used in the initial validation of the implementation. The authors are also grateful to Mike Steel for useful discussions and Michel Nevière and Evgeny Popov for their input regarding issues related to the dependence of the convergence on multipole order.

REFERENCES

1. J. K. Ranka, R. S. Windeler, and A. J. Stentz, "Optical properties of high-delta air-silica microstructure optical fibers," Opt. Lett. **25**, 796–798 (2000).
2. B. J. Eggleton, P. S. Westbrook, C. A. White, C. Kerbage, R. S. Windeler, and G. L. Burdge, "Cladding-mode resonances in air-silica microstructured optical fibres," J. Lightwave Technol. **18**, 1084–1100 (2000).
3. M. D. Feit and J. J. A. Fleck, "Computation of mode eigenfunctions in graded-index optical fibers by the propagating beam method," Appl. Opt. **19**, 2240–2246 (1980).
4. N. A. Issa and L. Poladian, "Vector wave expansion method for leaky modes of microstructured optical fibers," J. Lightwave Technol. **21**, 1005–1012 (2003).
5. T. P. White, B. T. Kuhlmey, R. C. McPhedran, D. Maystre, G. Renversez, C. Martijn de Sterke, and L. C. Botten, "Multipole method for microstructured optical fibers. I. Formulation," J. Opt. Soc. Am. B **19**, 2322–2330 (2002).
6. B. T. Kuhlmey, T. P. White, G. Renversez, D. Maystre, L. C. Botten, C. Martijn de Sterke, and R. C. McPhedran, "Multipole method for microstructured optical fibers. II. Implementation and results," J. Opt. Soc. Am. B **19**, 2331–2340 (2002).
7. E. Popov and M. Nevière, "Maxwell equations in Fourier space: a fast-converging formulation for diffraction by arbitrary shaped, periodic, anisotropic media," J. Opt. Soc. Am. B **18**, 2886–2894 (2001).
8. M. Nevière and E. Popov, *Light Propagation in Periodic Media* (Marcel Dekker, New York, 2003).
9. N. A. Issa, M. A. van Eijkelenborg, M. Fellew, F. Cox, G. Henry, and M. C. J. Large, "Fabrication and study of microstructured optical fibers with elliptical holes," Opt. Lett. **29**, 1336–1338 (2004).
10. A. W. Snyder and J. D. Love, *Optical Waveguide Theory* (Chapman & Hall, London, 1983).
11. W. Wijngaard, "Guided normal modes of two parallel circular dielectric rods," J. Opt. Soc. Am. **63**, 944–949 (1973).
12. K. M. Lo, R. C. McPhedran, I. M. Bassett, and G. W. Milton, "An electromagnetic theory of dielectric waveguides with multiple embedded cylinders," J. Lightwave Technol. **12**, 396–410 (1994).
13. C. Chang and H. Chang, "Theory of the circular harmonics expansion method for multiple-optical-fiber system," J. Lightwave Technol. **12**, 415–417 (1994).
14. M. Abramowitz and I. A. Stegun, *Handbook of Mathematical Functions* (Dover, New York, 1965).
15. L. Li, "Use of Fourier series in the analysis of discontinuous periodic structures," J. Opt. Soc. Am. A **13**, 1870–1876 (1996).
16. N. Issa, Optical Fibre Technology Centre, 206 National Innovation Centre, Australian Technology Park, Eveleigh New South Wales 1430, Australia, n.issa@oftc.usyd.edu.au (personal communication, 2003).
17. M. J. Steel and R. M. Osgood, Jr., "Elliptical-hole photonic crystal fibers," Opt. Lett. **26**, 229–231 (2001).
18. M. J. Steel and R. M. Osgood, Jr., "Polarization and dispersive properties of elliptical-hole photonic crystal fibers," J. Lightwave Technol. **19**, 495–503 (2001).
19. T. A. Birks, J. C. Knight, and P. St. J. Russell, "Endlessly single-mode photonic crystal fiber," Opt. Lett. **22**, 961–963 (1997).
20. J. C. Knight, T. A. Birks, and P. St. J. Russell, "Properties of photonic crystal fiber and the effective index model," J. Opt. Soc. Am. A **15**, 748–752 (1998).
21. B. T. Kuhlmey, R. C. McPhedran, C. Martijn de Sterke, and O. A. Robinson, "Microstructured optical fibers: where's the edge?" Opt. Express **10**, 1285–1290 (2002), http://www.opticsexpress.org.
22. H. Kubota, S. Kawanishi, S. Koyanagi, M. Tanaka, and S. Yamaguchi, "Absolutely single polarization photonic crystal fiber," IEEE Photonics Technol. Lett. **16**, 182–184 (2004).